View metadata, citation and similar papers at core.ac.uk
brought to you by CORE
provided by ScholarWorks@UNIST

The Astrophysical Journal, 620:21–30, 2005 February 10
© 2005. The American Astronomical Society. All rights reserved. Printed in U.S.A.

SHOCK-HEATED GAS IN THE LARGE-SCALE STRUCTURE OF THE UNIVERSE

Hyesung Kang,[1] Dongsu Ryu,[2] Renyue Cen,[3] and Doojong Song[4]
Received 2004 March 23; accepted 2004 October 18

ABSTRACT

Cosmological shock waves are a ubiquitous consequence of cosmic structure formation. They play a major role in heating baryonic gas in the large-scale structure of the universe. In this contribution we study the shock-heated gas in connection with shocks themselves, using a set of N-body/hydrodynamic simulation data of a ΛCDM universe. The distributions of shock speed and temperature of shock-heated gas should both reflect the depth of gravitational potential of associated nonlinear structures and thus their morphology. From their distributions we find, in addition to hot gas in and around clusters and groups and warm-hot intergalactic medium (WHIM) with $T = 10^5$–10^7 K, mostly in filaments, that there is a significant amount of low-temperature WHIM with $T < 10^5$ K distributed mostly as sheetlike structures. The low-temperature WHIM was heated and collisionally ionized mainly by shocks with $v_{\rm sh} \lesssim 150$ km s^{-1}, while photoionization by the UV and X-ray background radiation is important for metal ions. Not only the WHIM with $T = 10^5$–10^7 K but also the WHIM with $T < 10^5$ K makes up a significant fraction of gas mass, implying that the low-temperature WHIM could be important in resolving the missing-baryon problem. The shock-heated gas in filaments and sheets are manifested best through emission and absorption in the soft X-ray and far-UV bands. We confirm that the WHIM with $T = 10^5$–10^7 K makes significant contributions to the soft X-ray background, absorption of highly ionized species such as O vii and O viii in active galactic nucleus (AGN) spectra, and line emission from O vii and O viii ions, as pointed out by previous studies. However, the WHIM with $T < 10^5$ K is the major contributor to the absorption of lower ionized species such as O v and O vi, because these photoionized ions are most abundant in sheets of low density and temperature. On the other hand, lines of O v (630 Å) and O vi (1032 Å) are emitted mostly from the WHIM with $10^5 < T < 10^6$ K, because they are from collisionally excited ions.

Subject headings: cosmology: theory — diffuse radiation — large-scale structure of universe — methods: numerical — quasars: absorption lines — shock waves

Online material: color figures

1. INTRODUCTION

In the current paradigm of cold dark matter (CDM) cosmology, the large-scale structure of the universe has formed through hierarchical clustering of matter. Deepening of gravitational potential wells caused baryonic matter to accrete onto nonlinear structures. It has been postulated that the baryonic matter behaved like a gas and "collisionless shocks" formed in the tenuous, magnetized, cosmic plasma via collective electromagnetic viscosities (Kang et al. 1996; Quilis et al. 1998; Miniati et al. 2000; Gabici & Pasquale 2003; Ryu et al. 2003). In fact, the gravitational energy of the baryonic gas associated with structure formation was dissipated into heat primarily via such shocks. The dissipated energy then governs the thermal history and nature of the gas in the universe and reveals the large-scale structure as well as its dynamics through emitted radiation (Kang et al. 1994a; Cen et al. 1995; Cen & Ostriker 1999a; Davé et al. 2001; Valageas et al. 2002; Furlanetto & Loeb 2004).

In a recent work, Ryu et al. (2003) has studied the properties of "cosmological shock waves" and their roles in the thermalization of gas and acceleration of nonthermal particles in the large-scale structure, using cosmological N-body/hydrodynamic simulations. The cosmological shocks were classified into two types. "External shocks" form around outermost surfaces that encompass nonlinear structures, so they are by nature accretion shocks that decelerate the never-shocked intergalactic gas infalling toward sheets, filaments, and knots. "Internal shocks" are produced within those nonlinear structures by infall of previously shocked gas to filaments and knots, during subclump mergers, as well as by chaotic flow motions. External shocks have high Mach numbers of up to $M \sim 100$ because of the low temperature of the accreting gas. Internal shocks, on the other hand, have mainly low Mach numbers of $M \sim$ a few, because the gas inside nonlinear structures has been previously heated by shocks (external and/or internal) and so has a high temperature. However, internal shocks are more important in energetics because of higher preshock density. As a result, thermalization of gas and acceleration of cosmic rays occurs mostly at internal shocks.

The intergalactic gas was heated mostly by cosmological shock waves. The shock-heated gas with $T = 10^5$–10^7 K has been studied previously, utilizing cosmological hydrodynamic simulations (Cen & Ostriker 1999a; Davé et al. 2001). This component, called the warm-hot intergalactic medium (WHIM), was estimated to contain ∼30% of baryon mass at the present epoch and resides mostly in filaments with a median overdensity of ∼10–30. Such WHIM can account for a significant fraction of the missing baryons at low redshifts (Fukugita et al. 1998; Fukugita 2004). X-ray emission from the WHIM may contribute to a fraction of the soft X-ray background radiation (XBR) according to Phillips et al. (2001). While there were recent

[1] Department of Earth Sciences, Pusan National University, 30 Jangjeon-dong, Geumjeong-gu, Pusan 609-735, Korea; kang@uju.es.pusan.ac.kr.
[2] Department of Astronomy and Space Science, Chungnam National University, 220 Gung-dong, Yuseong-gu, Daejeon 305-764, Korea; ryu@canopus.chungnam.ac.kr.
[3] Princeton University Observatory, Princeton, NJ 08544; cen@astro.princeton.edu.
[4] Korea Astronomy Observatory, San 36-1 Whaam-dong, Yuseong-Gu, Taejeon 305-348, Korea; djsong@kao.re.kr.

reports of observations of the WHIM around clusters (see, e.g., Finoguenov et al. 2003; Zappacosta et al. 2004b), detection of such emission still remains a challenging task because of low surface brightness. On the other hand, the WHIM may be better detected through absorption systems and emission lines in soft X-ray and far-UV; for instance, the possibility of probing the WHIM with O VI absorbers has been explored by Cen et al. (2001) and Fang & Bryan (2001). Absorption systems due to other oxygen and metal ions in the intervening WHIM were studied by Hellsten et al. (1998), Chen et al. (2003), and Viel et al. (2003). Detections of such absorbers in X-ray observations including those from *Chandra* have been reported (see, e.g., Nicastro et al. 2003; McKernan et al. 2003, among many). Emission lines from metal ions in the WHIM were studied by Yoshikawa et al. (2003), Furlanetto et al. (2003), and Fang et al. (2005). A possible detection of such emission lines from a filament around the Coma Cluster has also been reported (Finoguenov et al. 2003).

In this paper, we study the shock-heated gas in the large-scale structure of the universe and evaluate its observational manifestations with data from a set of cosmological hydrodynamic simulations in which shock waves were identified (see Ryu et al. 2003). Specifically, the properties of shock-heated gas are analyzed in connection with those of cosmological shock waves. From the shock speed and gas temperature distributions, we see that (1) the shocks with $v_{\rm sh} \gtrsim 700$ km s^{-1} and the hot gas with $T > 10^7$ K are distributed in and around clusters and groups, (2) the shocks with $150 \lesssim v_{\rm sh} \lesssim 700$ km s^{-1} and the WHIM with $T = 10^5$–10^7 K are mostly in filamentary structures, and (3) the shocks with $v_{\rm sh} \lesssim 150$ km s^{-1} and the WHIM with $T < 10^5$ K are mostly in sheetlike structures. Here we refer the uncollapsed, collisionally ionized, shock-heated gas as the WHIM and extend the low-temperature bound of the WHIM to well below 10^5 K. While the WHIM with $T = 10^5$–10^7 K has been studied extensively in many previous works, the "low-temperature WHIM" with $T < 10^5$ K has not received much attention and will be the main subject of this study.

In § 2 simulation data are described along with numerical details. The properties of shock-heated gas are described in § 3, and its observational manifestations are discussed in § 4. A summary follows in § 5.

2. SIMULATION DATA

We used the data from a set of N-body/hydrodynamic simulations of a ΛCDM universe with radiative cooling. The simulations were performed using a PM+Eulerian hydrodynamic cosmology code that was specifically designed to capture shocks with a high accuracy. It is an updated version of the code described in Ryu et al. (1993). For instance, the code now adopts the MC (monotonized central difference) limiter instead of the original minmod limiter to achieve sharper resolution of discontinuities (see, e.g., LeVeque 1997). The ΛCDM model adopted the currently favored values of the following cosmology parameters for baryonic and dark matter: $\Omega_{\rm BM} = 0.043$, $\Omega_{\rm DM} = 0.227$, $\Omega_\Lambda = 0.73$ ($\Omega_{\rm BM} + \Omega_{\rm DM} + \Omega_\Lambda = 1$), $h \equiv H_0/(100 \text{ km s}^{-1} \text{ Mpc}^{-1}) = 0.7$, and $\sigma_8 = 0.8$. These values are consistent with those fitted with the recent *Wilkinson Microwave Anisotropy Probe* (*WMAP*) data (see, e.g., Bennett et al. 2003; Spergel et al. 2003). A cubic region of size $L = 100\ h^{-1}$ Mpc at present was simulated inside the computational box with 1024^3, 512^3, and 256^3 grid zones for gas and gravity and with 512^3, 256^3, and 128^3 particles for dark matter, allowing a "fixed" spatial resolution of $\Delta l = 97.7$–$390.6\ h^{-1}$ kpc. We note that the simulations of different resolution have exactly the same large-scale structure. The only difference is the Nyquist frequency in the initial condition, apart from spatial and mass resolutions.

We adopted the tabulated cooling rate that had been calculated by following the nonequilibrium collisional ionization of gas with a given metallicity, cooling from $10^{8.5}$ to 10^4 K under the isobaric condition (Sutherland & Dopita 1993). The radiative cooling rate based on equilibrium collisional ionization is not a good approximation for $T \lesssim 10^6$ K, since recombination lags cooling and so ionization fractions depend on the thermal and ionization history of the gas. The nonequilibrium cooling rate for the gas cooling under the isobaric condition, however, becomes a function of temperature only if the initial temperature is high enough to ensure the initial ionization equilibrium (e.g., $T \gtrsim 10^6$ K) and if only two-body collisional processes are included (see, e.g., Dopita & Sutherland 2003). In our simulations, gas was allowed to cool only down to $T \sim 10^4$ K and cooling was set equal to zero for $T < 10^4$ K. For void gas, the minimum temperature was set as the temperature of cosmic microwave background (CMB) radiation, i.e., $T_{\rm min} = T_{\rm CMB}(z)$. For metallicity, we adopted the mean metallicity-density relation

$$\frac{Z(\rho_{\rm gas})}{Z_\odot} = \min\left(0.3,\ \max\left(0.006, 0.03\left(\frac{\rho_{\rm gas}}{\bar{\rho}_{\rm gas}}\right)^{1/3}\right)\right), \quad (1)$$

which had been suggested by Cen & Ostriker (1999b), using the data from a cosmological simulation with feedback into the intergalactic medium (IGM) from stars. The simulations are the same ones previously used in Ryu et al. (2003) for the study of cosmological shock waves, except that radiative cooling is included.

We note a few points regarding numerical details. (1) Our simulations did not include star and galaxy formation and feedback from those stars, galaxies, and active galactic nuclei (AGNs), nor photoionization heating of the intergalactic gas. This is because our primary focus is the heating by cosmological shock waves and the properties of shock-heated gas in filaments and sheets. Nongravitational feedback is expected to be most important in high-density regions inside clusters and groups. Through previous studies by Cen & Ostriker (1999a) and Davé et al. (2001), it is known that the intergalactic gas was heated primarily by cosmological shock waves. Feedback may have contributed only ∼20% or so of the thermal energy of the intergalactic gas, so it should have played only a minor role in the thermal evolution of the WHIM in filaments and sheets. On the other hand, photoionization heating should have affected mostly diffuse gas in void regions and Lyα clouds, heating it to $T \sim 10^4$ K (see, e.g., Valageas et al. 2002). However, it should not have affected much the properties of the WHIM, since most of the WHIM has $T \gtrsim 10^4$ K in our simulations. When we estimated the amount of shock-heated gas, we excluded the components that would have been heated primarily by photoionization (see § 3 for details). However, the photoionization of metal ions, such as oxygen, by the background radiation was taken into account in postprocessing data analyses, since such photoionization dominates over collisional ionization for the WHIM in filaments and sheets. (2) Because of the fixed-grid–based nature, our data have a limitation in studies of high-density regions such as cores of clusters and

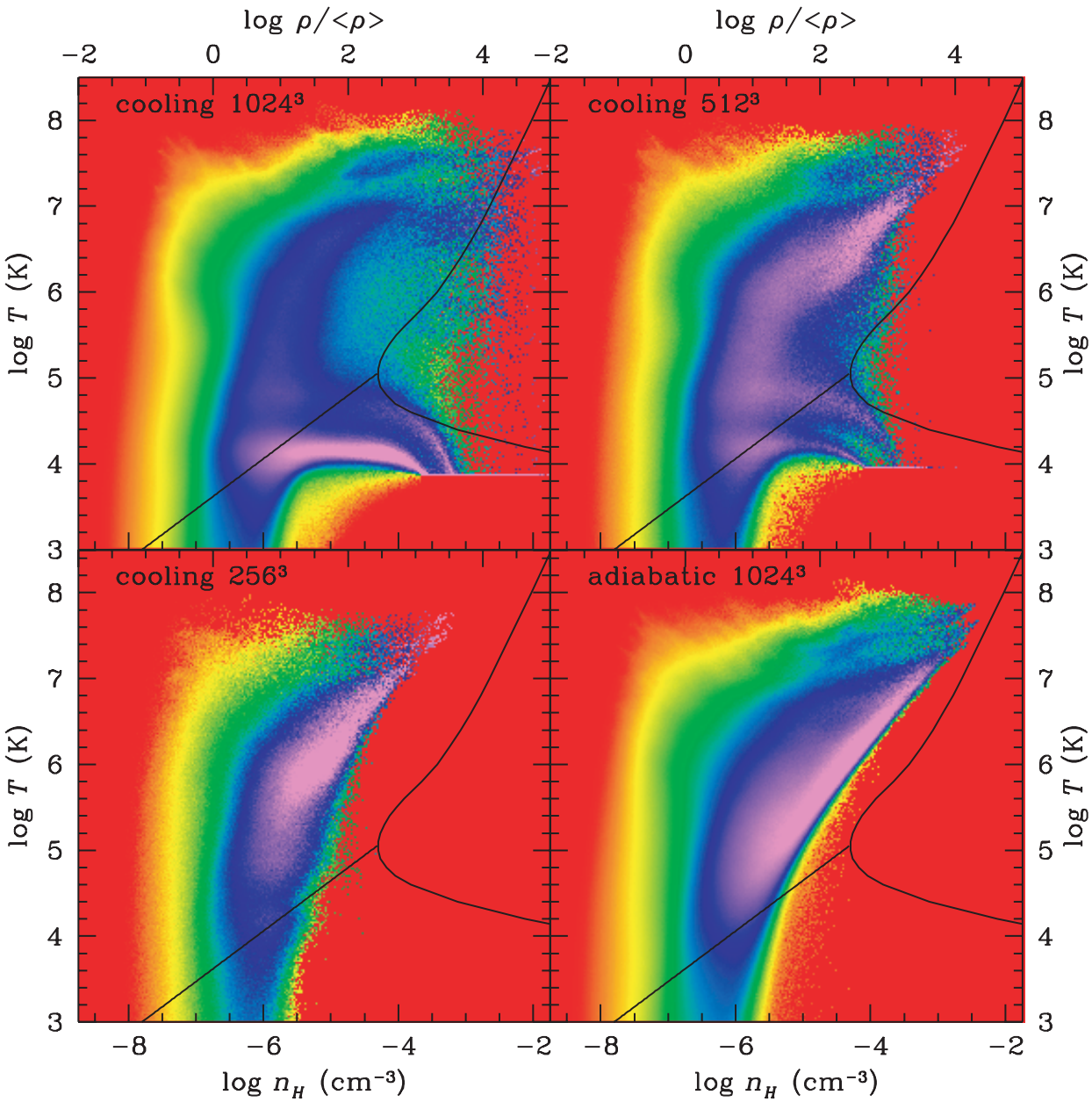

FIG. 1.—Mass distribution of shock-heated gas in the plane of gas density and temperature at $z = 0$ in simulations with different resolution. For comparison, the distribution from the 1024^3 simulation without cooling is also shown. Purple indicates the highest mass concentration, and the color scale was set arbitrarily to highlight the distribution. The black straight line presents the "Lyα equation of state," and the black curved line isolates the "fast-cooling" region of Valageas et al. (2002) (see text for details).

groups of galaxies, compared to those using SPH or AMR codes (Kang et al. 1994b; Frenk et al. 1999). However, the same fixed grid spacing turns out to be an advantage in studying the low-density gas in filaments and sheets. The typical thickness of filaments and sheets is $\sim 1\ h^{-1}$ Mpc or larger (see Fig. 2 below). In addition, the internal shocks inside those nonlinear structures have a mean separation of $\sim 1\ h^{-1}$ Mpc (Ryu et al. 2003). As shown below, numerical resolution is important in studies of the gas inside those nonlinear structures. The fixed grid spacing of $\Delta l = 97.7\ h^{-1}$ kpc, $\sim 1/10$ of those scales in our highest resolution simulation seems to be good enough to resolve filaments and sheets and shocks in those structures (Ryu et al. 2003). (3) In order to establish the connection between shock-heated gas and cosmological shocks, we identified shock surfaces by the procedure described in Ryu et al. (2003). Only the shocks with $v_{\rm sh} \geq 15$ km s^{-1} were identified, although the code itself captures shocks of any speed.

3. SHOCK-HEATED GAS IN FILAMENTS AND SHEETS

3.1. *Temperature and Density of Shock-heated Gas*

We begin our discussion with the temperature and density of shock-heated gas in the simulated universe. Figure 1 shows the mass distribution in the plane of gas density and temperature at $z = 0$ from different simulations. The purple line along $T \sim 10^4$ K in the high-density regime in the simulations with 1024^3 and 512^3 grid zones is an artifact of numerical simulation. In order to isolate the shock-heated WHIM, we draw two lines in

TABLE 1
Mass Fractions of Shock-heated Gas

Component	1024^3	512^3	256^3
Hot with $T > 10^7$ K[a]	0.022	0.024	0.029
WHIM with $T = 10^5$–10^7 K	0.24	0.37	0.43
WHIM with $T < 10^5$ K	0.13	0.13	0.10

[a] The gas within 1 h^{-1} Mpc of clusters and groups hotter than 1 keV was not counted.

the figure. The straight line represents the "Lyα equation of state" of Valageas et al. (2002),

$$T_\alpha = 0.418\times10^4\left(\frac{\rho_{\rm gas}}{\bar{\rho}_{\rm gas}}\right)^{0.59}, \qquad (2)$$

which was adjusted for different values of cosmological parameters employed (see also Hui & Gnedin [1997], among many references). The line comes from the interplay of radiative heating by the UV background with the expansion of the universe. The region of overdensity $\delta \lesssim 10$ that lies below this line would have been heated primarily by the background UV radiation to the temperature depicted by the line. The curved line in the high-density regime delineates the "fast-cooling" dense region, which was adopted also from Valageas et al. (2002), again with a suitable modification due to different values of parameters. It comes from the equality of the effective cooling time due to radiative cooling plus heating by the background UV radiation and the Hubble time. The high-density region ($\delta \gtrsim 10$) below the Lyα line and right to the fast-cooling line would have been collapsed into objects such as stars and galaxies or would be in the form of bound objects, if the resolution were not limited by fixed grid spacing in our simulations (see, e.g., Furlanetto et al. [2003], for the distribution of gas from an SPH simulation). Since our focus is on the intergalactic gas that was mainly heated by shock waves, we exclude in our discussion and analyses below the photo-heated gas as well as the gas in collapsed or bound objects.

Several points are apparent in Figure 1. (1) In addition to the hot component with $T > 10^7$ K and the WHIM with $T = 10^5$–10^7 K, which were discussed in previous studies of shock-heated gas (Cen & Ostriker 1999a; Davé et al. 2001), there exists a significant amount of low-temperature WHIM in the range of $T < 10^5$ K. The mass fraction of the gas in each component is ~2.2% in the hot component, ~24% in the WHIM with $T = 10^5$–10^7 K, and ~13% in the WHIM with $T < 10^5$ K in our highest resolution simulation data (see Table 1). In the hot component, the gas within 1 h^{-1} Mpc of clusters and groups hotter than 1 keV was not included. Most of the low-temperature WHIM has the temperature of 10^4 K $< T < 10^5$ K, while the mass of the WHIM with $T < 10^4$ K is ~3% of total gas mass. (2) Our estimate of mass fraction for the WHIM with $T = 10^5$–10^7 K is comparable to, although a little smaller than, ~30% from simulations using the PTreeSPH and AMR codes (Davé et al. 2001). A part of the difference would be due to feedback from stars, galaxies, and AGNs, which were ignored in our simulations. (3) It is interesting to note that the distribution of our WHIM follows very closely the "equation of state for the warm IGM" analytically suggested by Valageas et al. (2002). However, their estimation of the mass fraction for the "warm IGM," ~24%, is somewhat smaller than our estimation for all the WHIM with $T < 10^7$ K. (4) Gas density reaches to higher values and cooling becomes even more efficient with the ρ^2 dependence at higher resolution. The resulting trend is that there is more gas with high density and low temperature in higher-resolution simulations. As a result, the mass fraction of the WHIM continues to decrease as resolution increases in our simulations (see Table 1).

3.2. *Spatial Distributions of Shock Waves and Shock-heated Gas*

In this subsection, we investigate the spatial distribution of shock-heated gas in conjunction with that of shock waves themselves. As mentioned in the introduction, two types of shocks can be distinguished. "External shocks" are accretion shocks around nonlinear structures, whose speed is basically the infall velocity of accreting flows. "Internal shocks" are products of infall, merging, and chaotic flow motions induced by gravitational interactions inside nonlinear structures. So the shock speed of both types should reflect the depth of gravitational potential wells of nonlinear structures and hence their morphology. In our simulations, (1) high-speed shocks with $v_{\rm sh} \gtrsim 700$ km s^{-1} are found mostly around and inside knotlike structures of clusters and groups, (2) shocks with 150 km s^{-1} $\lesssim v_{\rm sh} \lesssim 700$ km s^{-1} are found mostly around and inside filamentary structures, and (3) low-speed shocks with $v_{\rm sh} \lesssim 150$ km s^{-1} are found mostly around and inside sheetlike structures. The left panels of Figure 2 show the locations of external shocks, divided into the three speed groups, in a two-dimensional slice at $z = 0$ from the 1024^3 simulation. The shocks encompass and outline nonlinear structures. The structures with width of ~1 h^{-1} Mpc in the top left panel are mostly sheetlike structures with shallow potentials, while the thicker structures with width of $\gtrsim 2$ h^{-1} Mpc in the middle left panel are filaments (see also Fig. 3 below). The structure in the bottom left panel contains a cluster with X-ray emission-weighted temperature $T_{\rm X} \approx 2.4$ keV and X-ray luminosity $L_{\rm X} \approx 4.1\times10^{45}$ h ergs s^{-1} (note that this cluster has a high luminosity for its temperature due to excessive cooling without feedback from stars and galaxies).

The morphological distinction can be revealed more clearly in three-dimensional volume renderings for the distribution of shocks waves. The image in Figure 3*a* displays all shocks (external and internal) inside the full box of (100 h^{-1} Mpc)^3. At a quick glance, filamentary structures look dominant. However, a careful inspection, especially near the edges of the box where structures do not overlap, exhibits many sheetlike structures. In order to take a close look at sheetlike structures, we show in Figures 3*c* and 3*d* the distribution of low-speed shocks with $v_{\rm sh} < 150$ km s^{-1} in a region of (25 h^{-1} Mpc)^3, which is marked in the top left panel of Figure 2. For filamentary structures we show in Figures 3*e* and 3*f* the distribution of shocks with 150 km s^{-1} $< v_{\rm sh} <$ 700 km s^{-1} in a region of (31 h^{-1} Mpc)^3, which is marked in the middle left panel of Figure 2. For further reference, volume rendering movies for shocks of different speed groups in the two regions shown in Figure 3*c*–3*f* as well as in the region covering the complex in the bottom left panel of Figure 2 are available on the authors' Web page.[5] The figures (along with the movies) demonstrate that the morphology of nonlinear structures can be revealed through the distributions of shocks of the three speed groups.

Naturally, it is expected that the spatial distribution of shock-heated gas is closely related to that of cosmological shock waves.

[5] The movies are posted at http://canopus.chungnam.ac.kr/ryu/shock.html.

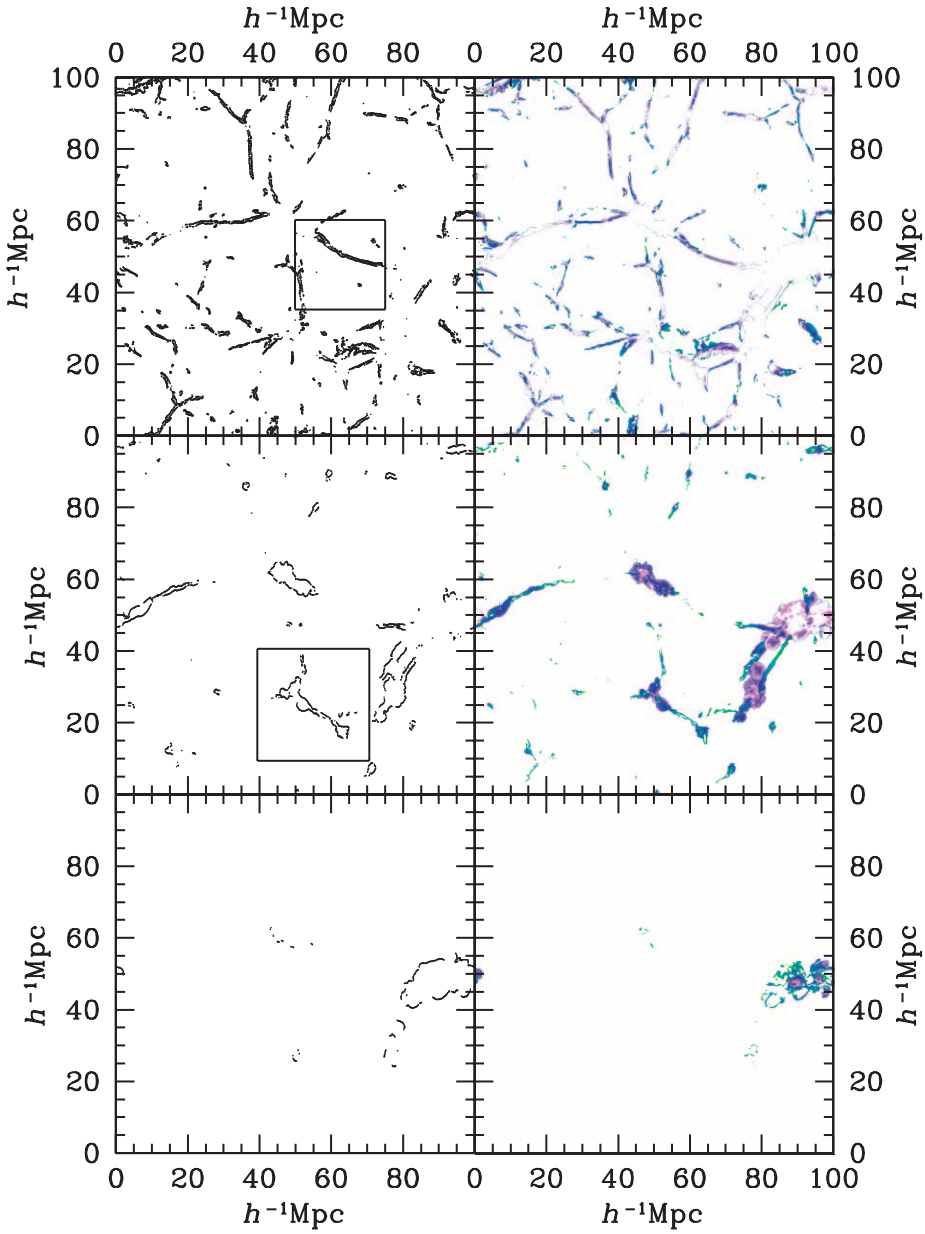

FIG. 2.—*Left panels*: Locations of external shocks at $z = 0$ in a two-dimensional slice of $(100\ h^{-1}\ \mathrm{Mpc})^2$ from the 1024^3 simulation. The shocks are classified into three groups according to shock speed, $v_{\rm sh} < 150$ km s^{-1}, 150 km s^{-1} $< v_{\rm sh} <$ 700 km s^{-1}, and $v_{\rm sh} > 700$ km s^{-1}, respectively, from top to bottom. *Right panels*: Spatial distribution of shock-heated gas at $z = 0$ in the same slice in three ranges of temperature: the WHIM with $T < 10^5$ K, the WHIM with $T = 10^5$–10^7 K, and the hot component with $T > 10^7$ K, shown in the top, middle, and bottom panels, respectively. In each panel purple represents the gas with temperature close to the upper bound, green represents gas close to the lower bound, and blue represents gas in the middle.

Figure 3*b* shows a three-dimensional volume rendering image for the temperature of shock-heated gas in the same perspective as that of Figure 3*a*. The images confirms that the two distributions are indeed very similar. The right panels of Figure 2 show the gas distribution in three temperature ranges, 10^3 K $< T < 10^5$ K, 10^5 K $< T < 10^7$ K, and $T > 10^7$ K, in the same two-dimensional slice as in the left panels. With the choice of temperature ranges, the different morphology defined by shock waves is revealed once again by gas temperature as well, i.e., the hot component mostly in knotlike structures, the WHIM with $T = 10^5$–10^7 K mostly in filaments, and the low-temperature WHIM with $T < 10^5$ K mostly in sheetlike structures. Hence, our results suggest the existence of a component of the intergalactic gas, the low-temperature WHIM with $T < 10^5$ K, that has not been explored in detail in previous studies.

4. SHOCK-HEATED GAS IN OBSERVATIONS

4.1. *X-Ray Emission from Shock-heated Gas*

As noted in the introduction, it has been suggested that the X-ray emission from the WHIM may contribute significantly to the soft XBR. Phillips et al. (2001) estimated that the emission would contribute ~10% of the observed XBR in the 0.5–2 keV range. They used ΛCDM simulation data in which radiative cooling, feedback from galaxies, and photoionization were included, and 512^3 grid zones were used for the box of 100 h^{-1} Mpc size. On the other hand, based on analyses of observational data, Zappacosta et al. (2004a) suggested that most of the soft XBR could come from the WHIM. In order to assess how numerical details, including finite resolution, would affect the prediction, we calculated the X-ray emission from the

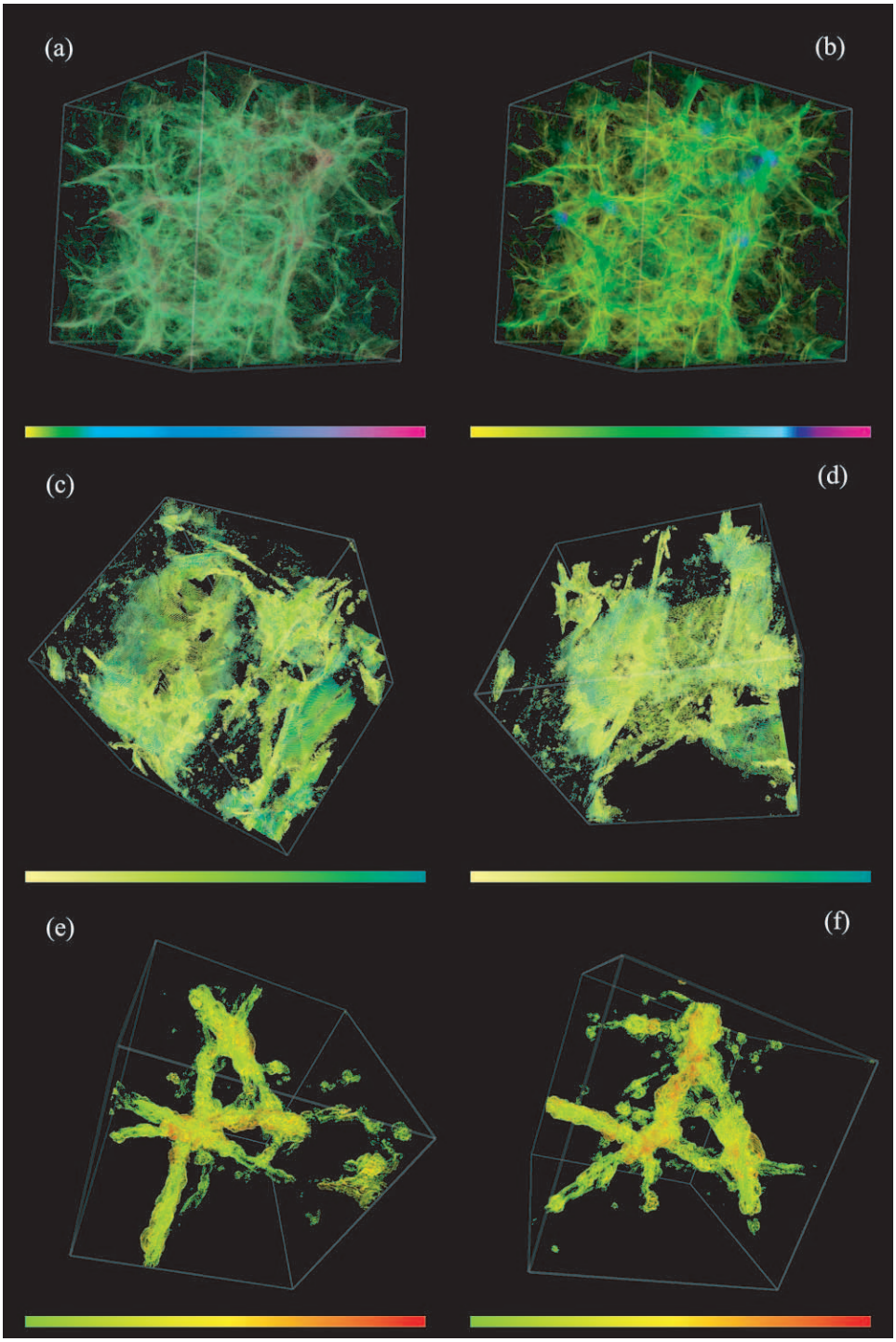

FIG. 3.—(*a*) Distribution of shock waves (external and internal) at $z = 0$ in the full box of $(100\ h^{-1}\ \mathrm{Mpc})^3$. Color represents logarithmically scaled shock speed from $v_{\rm sh} = 15$ km s^{-1} (*yellow*) to 1500 km s^{-1} (*purple*) and higher. (*b*) Temperature distribution of shock-heated gas at $z = 0$ in the same box. Color covers logarithmically scaled temperature from $T = 10^4$ K (*yellow*) to 10^8 K (*purple*) and higher. (*c*, *d*) Distribution of shock waves (external and internal) with $v_{\rm sh} = 15$ km s^{-1} (*yellow*) to 150 km s^{-1} (*blue-green*) at $z = 0$ in a region of $(25\ h^{-1}\ \mathrm{Mpc})^3$, marked at the top left panel of Fig. 2. Two different perspectives are shown. (*e*, *f*) Distribution of shock waves (external and internal) with $v_{\rm sh} = 150$ km s^{-1} (*green*) to 700 km s^{-1} (*red*) at $z = 0$ in a region of $(31\ h^{-1}\ \mathrm{Mpc})^3$, marked at the middle left panel of Fig. 2. Two different perspectives are shown. All images are from the 1024^3 simulation.

shock-heated gas outside clusters and groups using our simulation data with 1024^3, 512^3, and 256^3 grid zones. As in Phillips et al. (2001), the gas in spherical regions of 1 h^{-1} Mpc radius around clusters and groups with $T_{\rm X} \geq 1$ keV was excluded, since they would be identified as discrete X-ray sources and be removed from contributors to the background radiation. In addition, the gas below the Lyα and fast-cooling lines in Figure 1 was excluded. The X-ray spectrum code for an optically thin gas, MEKAL (Mewe et al. 1985), was used to calculate the mean proper volume emissivity, $\epsilon(E, z)$, from the entire simulation box at $z = 2$, 1.5, 1, 0.5, 0.2, and 0. The mean background intensity at $z = 0$, $J(E)$, was calculated then by integrating $\epsilon(E, z)$ from $z = 2$ to 0. In addition, the energy flux, $dF/d\log T$, in the X-ray band of 0.5–2 keV from the gas with

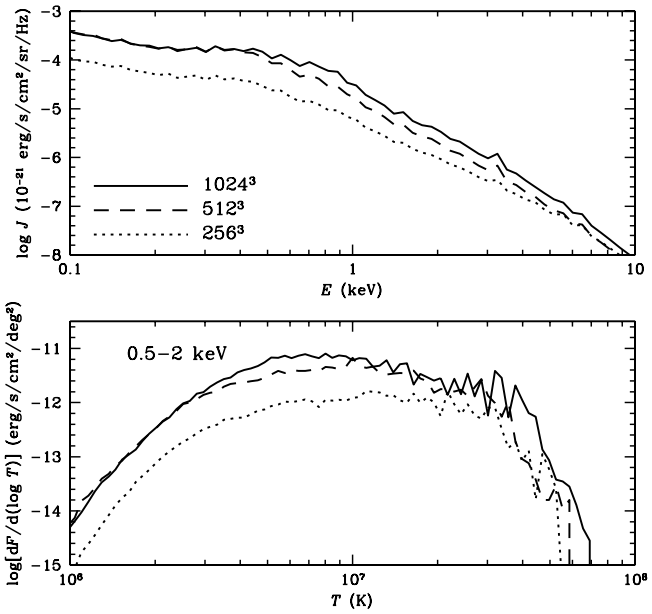

FIG. 4.—*Top*: Mean background intensity in soft X-ray from shock-heated gas, integrated from $z = 2$ to 0, in simulations with different resolution. *Bottom*: X-ray flux in the 0.5–2 keV energy band from shock-heated gas as a function of temperature, integrated from $z = 2$ to 0, in the same simulations. The gas in spheres of a radius 1 h^{-1} Mpc around clusters and groups hotter than 1 keV was excluded in calculating the X-ray radiation. [*See the electronic edition of the Journal for a color version of this figure*.]

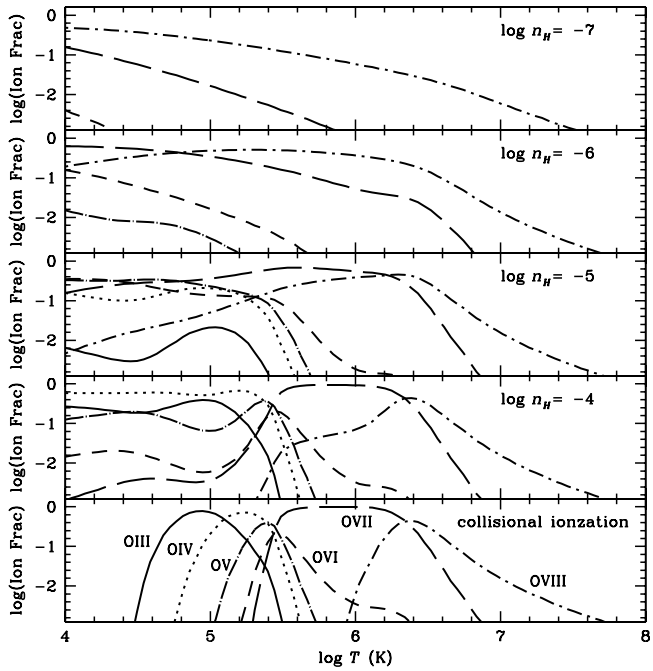

FIG. 5.—Fractions of O III to O VIII ions as a function of temperature for the gas of hydrogen number density $\log(n_{\rm H}) = -7$ to -4. Collisional ionization as well as photoionization by the UV and X-ray background radiation (Miyaji et al. 1998; Shull et al. 1999) were included. For comparison, the fractions of the ions in collisional ionization equilibrium are also shown. [*See the electronic edition of the Journal for a color version of this figure*.]

temperature between $\log T$ and $\log T + d\log T$ was calculated from the proper volume emissivity, $\epsilon(E, T, z)$, as in the calculation of $J(E)$. The top and bottom panels of Figure 4 show $J(E)$ and $dF/d\log T$, respectively, from the simulation data of different resolution.

Two points are noticed in Figure 4. (1) From the bottom panel, we confirm that among the shock-heated gas, it is the WHIM with $T \sim 5\times(10^6\text{–}10^7)$ K that contributes the most to the soft XBR. (2) The amount of X-ray emission increases with resolution, although the amount of shock-heated gas that emits such radiation decreases (see Table 1). This is because there is systematically more gas with higher density in higher resolution simulations. The X-ray emission in our two high-resolution simulations (1024^3 and 512^3) differs by only a factor of 2 or so in $E \gtrsim 0.5$ keV. The fractional contribution to the observed XBR (see Phillips et al. [2001] for discussions on observations) is largest in the 0.5–1 keV range and estimated to be ~30% in the 1024^3 simulation and ~15% in the 512^3 simulation. Our estimation from the 512^3 simulation is comparable to, although a little larger than, the ~10% of Phillips et al. (2001), which has the same spatial resolution. Although our simulations and that in Phillips et al. (2001) were performed with the same numerical code, different treatments of additional physical processes as well as details of numerical schemes should have led to the difference. However, our estimation from the highest resolution simulation with 1024^3 grid zones is ~3 times larger than theirs, indicating that the WHIM could be a major contributor to the soft XBR.

4.2. *Absorption Systems of Shock-heated Gas*

It has been suggested that the properties of the shock-heated gas in filaments and sheets may be studied best by analyzing the soft X-ray and far-UV "absorption systems" or "X-ray forests" in the spectra of distant quasars and AGNs. In particular, the O VI absorption systems in far-UV and the O VII and O VIII absorption systems in soft X-ray have been studied extensively by several authors (see § 1 for references). We also study the properties of such absorbers in our simulated local universe at $z = 0$, following the procedure described below. First, we constructed a table for the fractions of oxygen ions as a function of gas temperature and density. Since photoionization of oxygen ions is important for the low-density gas in filaments and sheets, the X-ray background radiation of Miyaji et al. (1998) and the UV background radiation of Shull et al. (1999) were included, following Chen et al. (2003). The photoionization code CLOUDY (Ferland et al. 1998) was used to compute the fractions of oxygen ions in a grid of temperature and density. Figure 5 shows the resulting fractions of oxygen ions at hydrogen number density $-7 \leq \log n_{\rm H} \leq -4$ as a function of temperature. For comparison, the fractions when no ionizing background radiation is present are also shown. It is obvious that the photoionization of oxygen ions by the adopted background radiation is very significant in the temperature range that corresponds to filaments and sheets ($T < 10^7$ K). The most noticeable point is that, with the ionizing background radiation, the fractions of highly ionized oxygen ions increase at lower density. According to Figure 1 the WHIM have the hydrogen number density, $-6 \lesssim \log n_{\rm H} \lesssim -5$, so the fractions of O VI, O VII, and O VIII ions are highest in those components. This is one of the reasons why these oxygen ions were studied extensively in previous works.

Next we calculated the column density distributions of absorption systems due to these oxygen ions. In simulation data, clouds of shock-heated gas were identified along the $N_{\rm lp} = 3N_g^2$ (N_g is the number of grid zones in one direction) line paths of $L = 100\ h^{-1}$ Mpc at $z = 0$. Again, the gas in spherical regions of 1 h^{-1} Mpc radius around clusters and groups with $T_{\rm X} \geq 1$ keV as well as the gas below the Lyα and fast-cooling

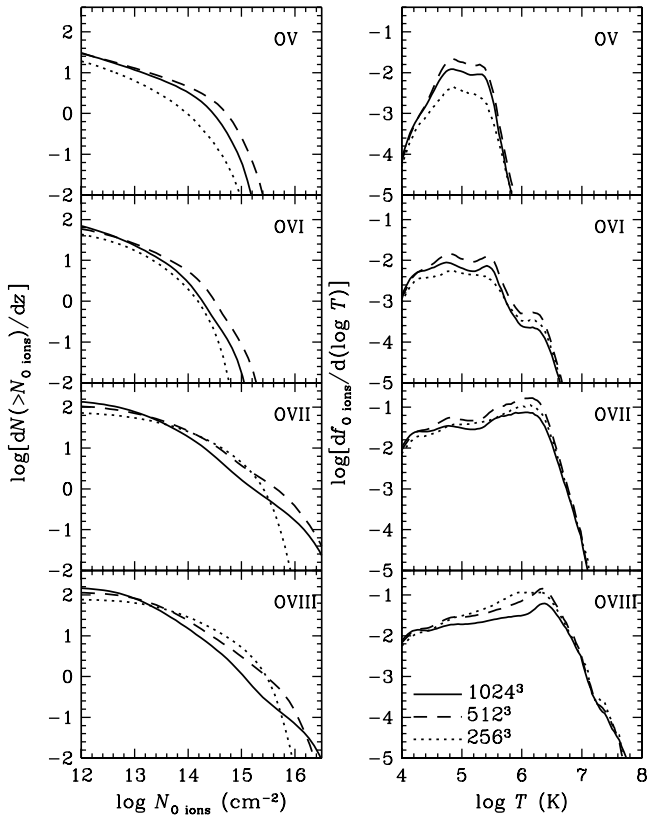

FIG. 6.—*Left panels*: Number of absorption lines per unit redshift by intervening gas clouds at $z = 0$ with the column density of oxygen ions larger than $N_{\rm O\ ions}$. *Right panels*: Fractions of O V–O VIII ions relative to the total oxygen abundance in shock-heated gas at $z = 0$ as a function of temperature. [*See the electronic edition of the Journal for a color version of this figure*.]

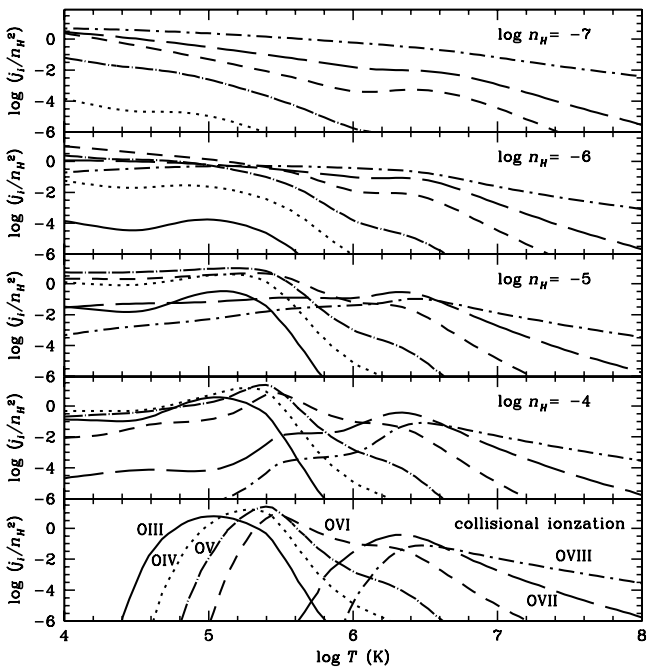

FIG. 7.—Emissivity of O III to O VIII ion lines as a function of temperature for the gas of hydrogen number density $\log(n_{\rm H}) = -7$ to -4: O III (698 Å), O IV (549 Å), O V (630 Å), O VI (1032 Å), O VII (574 eV), O VIII (653 eV). The term $j_i/n_{\rm H}^2$ is in units of 10^{-24} ergs cm^3 s^{-1}. Collisional ionization as well as photoionization by the UV and X-ray background radiation (Miyaji et al. 1998; Shull et al. 1999) were considered. For metallicity, $Z = 0.1\ Z_\odot$ was set. For comparison, the emissivity of the ion lines in collisional ionization equilibrium is also shown. [*See the electronic edition of the Journal for a color version of this figure*.]

lines were excluded. The metallicity was assigned at each grid zone according to equation (1). The left panels of Figure 6 show the cumulative distributions of absorption system column density for O V–O VIII ions,

$$\frac{dN(>N_{\rm O\ ions})}{dz} = \frac{N_{\rm abs}(>N_{\rm O\ ions})}{\Delta z}, \qquad (3)$$

where $N_{\rm abs}$ is the number of absorption lines with column density, $N_{\rm O\ ions}$, greater than given values. As expected from Figure 5, the O VII and O VIII absorption systems are strongest. In the 1024^3 simulation data, $dN/dz \sim 1$ for both $N_{\rm O\ VII}$ and $N_{\rm O\ VIII} \geq 10^{15}$ cm^{-2}, which is in good agreement with Chen et al. (2003) and Viel et al. (2003). The column densities of O V and O VI ions are smaller, so $dN/dz \sim 1$ for $N_{\rm O\ V} \gtrsim 3 \times 10^{14}$ cm^{-2} and $N_{\rm O\ VI} \gtrsim 2 \times 10^{14}$ cm^{-2}. We note that the column density distributions in the 1024^3 and 512^3 simulation data converge within a factor of 2.

The right panels of Figure 6 show the mass fractions of O V–O VIII ions due to the gas with temperature between $\log T$ and $\log T + d\log T$,

$$\frac{df_{\rm O\ ions}(T)}{d\log T} = \frac{1}{\mathcal{M}_{\rm O}}\frac{d\mathcal{M}_{\rm O\ ions}(T)}{d\log T}, \qquad (4)$$

which was normalized with the total oxygen mass $\mathcal{M}_{\rm O}$. We find that the WHIM with $T = 10^5$–10^7 K contributes to most of the absorption systems of O VII (~70%) and O VIII (~80%). Hence, the observations of those absorption systems would explore filamentary structures, as pointed out in Viel et al. (2003). However, the low-temperature WHIM with $T < 10^5$ K is the major contributor to the O V and O VI absorption systems, accounting for ~55% and ~60%, respectively. This emphasizes the importance of the low-temperature WHIM in some observations, as noted by Bergeron et al. (2002) in the study of O VI systems in a quasar spectrum.

4.3. *Emission Lines from Shock-heated Gas*

Observations of emission lines from the shock-heated gas in filaments and sheets still remain technically challenging. However, it has been suggested that detections of such emission could be possible with future X-ray missions such as the *Missing Baryon Explorer* (*MBE*)[6] and *Diffuse Intergalactic Oxygen Surveyor* (*DIOS*; Ohashi et al. 2004). In this subsection, we study the oxygen emission lines radiated by the WHIM in our simulation data. First, a table for the emissivity of O III (698 Å), O IV (549 Å), O V (630 Å), O VI (1032 Å), O VII (574 eV), and O VIII (653 eV) lines was constructed on a grid of gas temperature and density using CLOUDY (Ferland et al. 1998). Collisional ionization as well as photoionization due to the UV and X-ray background radiation described in § 4.2 were included. Figure 7 shows the resulting emissivity from the optically thin gas of hydrogen number density $-7 \leq \log n_{\rm H} \leq -4$. For comparison, the emissivity when no ionizing background radiation is present is also shown. From this figure one can expect that for $T > 10^6$ K the strongest lines from the gas with $-6 \lesssim \log n_{\rm H} \lesssim -5$ in filaments and sheets (see Fig. 1) would be the

[6] See http://www.ssec.wisc.edu/baryons/.

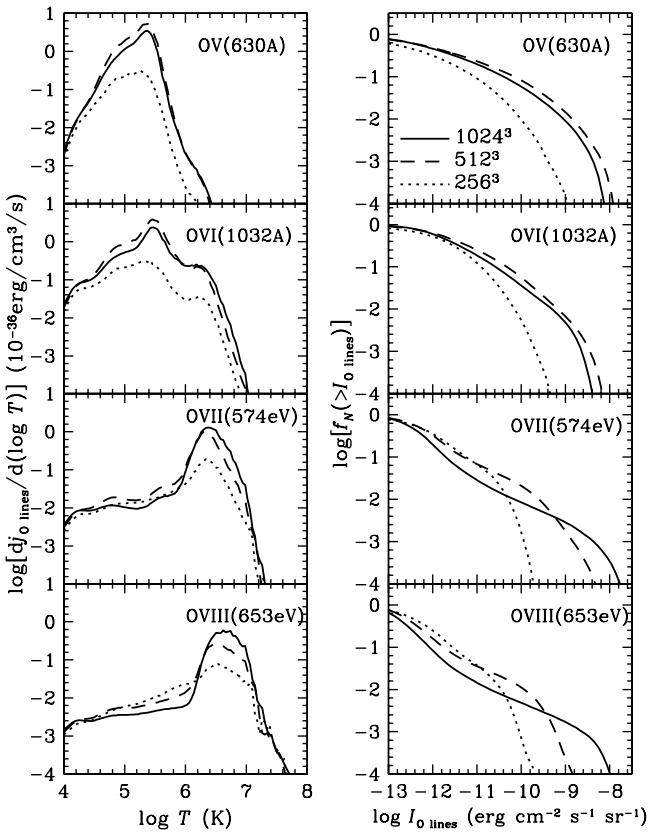

FIG. 8.—*Left panels*: Mean emissivity of O V to O VIII lines from shock-heated gas at $z = 0$ as a function of temperature. *Right panels*: Cumulative fraction of line paths with the specific intensity of oxygen lines larger than $I_{\rm O\ lines}$. The intensity was calculated by integrating the emissivity divided by 4π along a length of 100 h^{-1} Mpc at $z = 0$. [*See the electronic edition of the Journal for a color version of this figure.*]

O VII and O VIII lines. However, for $T < 10^6$ K, O V and O VI would produce emission lines stronger than O VII and O VIII lines.

Using the emissivity table, the oxygen line emissivity from the gas in simulation data was calculated at $z = 0$. As in the calculation of absorption column density, only the shock-heated gas was included and the same metallicity-density relation was adopted. The left panels of Figure 8 show the mean emissivity, $j_{\rm O\ lines}$, of O V–O VIII lines from the gas with temperature between $\log T$ and $\log T + d\log T$. Overall, the strength is greatest for the O V and O VI lines, followed by the O VII and O VIII lines. While virtually all emission of the O VII and O VIII lines come from the higher temperature WHIM with 10^6 K $< T < 10^7$ K ($\sim$95% for both lines), the O V and O VI lines are emitted mostly from the WHIM with 10^5 K $< T < 10^6$ K, $\sim$75% and $\sim$80%, respectively. Unlike the O V and O VI absorptions, which get significant contributions from the WHIM with $T < 10^5$ K, the line emission of O V (540 Å) and O VI (1032 Å) comes mostly from the WHIM with $T > 10^5$ K. Our estimates of line emission converge again within a factor of 2 in the 1024^3 and 512^3 simulation data.

Our results indicate that the exploration of shock-heated gas through emission in soft X-rays, such as the *MBE* and *DIOS* missions, would pick up a fraction of the WHIM with 10^6 K $\lesssim T \lesssim 10^7$ K ($\sim$10% of total gas mass in our estimate), missing the lower temperature WHIM with $T \lesssim 10^6$ K. A search using the O V and O VI line emission in far-UV would detect a larger fraction of the low-temperature WHIM with 10^5 K $\lesssim T \lesssim 10^6$ K ($\sim$14% of total gas mass), complementing the proposed missions in the soft X-ray band.

We also calculated the specific intensity of oxygen lines, $I_{\rm O\ lines}$, by integrating the emissivity/4π along columns of 100 h^{-1} Mpc at $z = 0$. Note that the Hubble expansion speed over the scale of 100 h^{-1} Mpc is $(1/30)c$, and the angular size of a single grid of Δl at a distance of $L = 100\ h^{-1}$ Mpc is $\Delta l/L$ radian. Thus, $I_{\rm O\ lines}$ corresponds effectively to the intensity measured over a band of width $\Delta\lambda/\lambda \sim 1/30$ with a beam of solid angle $3'.4 \times 3'.4$ or smaller when computed with the 1024^3 simulation data. We integrated along $N_{\rm lp} = 3N_g^2$ different line paths in the simulation box. The right panels of Figure 8 show the cumulative fraction of line paths with $I_{\rm O\ lines}$ larger than given values. They show that the fraction of randomly chosen line paths with $I_{\rm O\ lines} \geq 10^{-9}$ ergs cm^{-2} s^{-1} sr^{-1} would be $\sim 10^{-2}$ for the O V and O VI lines, while it would be $(2\text{–}3) \times 10^{-3}$ for the O VII and O VIII lines. However, the fraction of $I_{\rm O\ lines} \geq 10^{-8}$ ergs cm^{-2} s^{-1} sr^{-1} is $f_N \sim (1\text{–}2) \times 10^{-4}$ for the O VII and O VIII lines and larger than that for the O V and O VI lines. This reflects the fact that while the O V and O VI lines are stronger overall, the O VII and O VIII lines are from the WHIM with $T \gtrsim 10^6$ K and density higher than the mean density of shock-heated gas.

5. SUMMARY

Hierarchical clustering induces cosmological shock waves in the course of large-scale structure formation in the universe (Ryu et al. 2003). The intergalactic gas was heated mostly by such shocks (Cen & Ostriker 1999a; Davé et al. 2001; Valageas et al. 2002). In this paper, we study the properties, spatial distribution, and possible observational manifestations of the shock-heated gas in filaments and sheets with a set of simulation data of a ΛCDM universe from a grid-based *N*-body/hydrodynamic code (Ryu et al. 1993). The nature of fixed grid spacing makes such data suitable for studying the shock-heated gas in filaments and sheets. Shock heating is focused, so feedback from stars, galaxies, and AGNs and photoionization heating is ignored, although the photoionization of metal ions by the background radiation is taken into account in postprocessing data analyses. We expect that the exclusion of such processes should not significantly weaken the main results of this work, since the gas in filaments and sheets was heated mostly by cosmological shocks.

The speed of cosmological shock waves reflects the depth of gravitational potential of the associated nonlinear structures and thus their morphology. We see that (1) the shocks with $v_{\rm sh} \gtrsim 700$ km s^{-1} are distributed mostly around and inside clusters and groups, (2) the shocks with 150 km s$^{-1} \lesssim v_{\rm sh} \lesssim 700$ km s^{-1} are found mostly around and inside filamentary structures, and (3) the shocks with $v_{\rm sh} \lesssim 150$ km s^{-1} are found mostly around and inside sheetlike structures. The distribution of the shock-heated gas should be closely related to that of shock waves. We find that the WHIM with $T = 10^5$–10^7 K is distributed mostly in filamentary structures, while the low-temperature WHIM with $T < 10^5$ K is mostly in sheetlike structures. The hot gas with $T > 10^7$ K resides on knotlike structures as the intracluster and intragroup medium and the low-density medium around them. The amount of shock-heated gas is estimated as follows: the hot component with $T > 10^7$ K (excluding the gas inside clusters and groups) accounts for $\sim$2.2% of total gas mass, the WHIM with $T = 10^5$–10^7 K for $\sim$24%, and the WHIM with $T < 10^5$ K for $\sim$13% in our highest resolution simulation. Thus, our results indicate the existence of the WHIM with $T < 10^5$ K, which was heated by low-speed

shocks with $v_{sh} \lesssim 150$ km s^{-1} and is distributed as sheetlike structures. We suggest that *the low-temperature WHIM with* $T < 10^5$ K *contributes to a significant fraction of the missing baryons at low redshifts* (Fukugita et al. 1998; Fukugita 2004).

It has been suggested in previous studies (see § 1 for references) that the shock-heated gas in filaments and sheets can be manifested through emission and absorptions in the soft X-ray and far-UV. (1) We find that the soft X-ray emission from the shock-heated gas in our highest resolution data contributes to ~30% of the observed XBR in the 0.5–1 keV range. This is somewhat larger than that previously suggested by Phillips et al. (2001). (2) Column densities of oxygen ions along randomly selected line paths in the computational box were calculated. Such column densities can produce the absorption systems or X-ray forests in the spectra of distant quasars and AGNs (see, e.g., Hellsten et al. 1998). The photoionization of oxygen ions by the background UV and X-ray radiation is important for the gas in filaments and sheets because of low density and temperature. As a result, the fraction of oxygen ions depends strongly on the local gas density. We find that, for O VII and O VIII, the absorption systems associated with the WHIM with $T = 10^5$–10^7 K account for 70%–80% of the identified absorption systems, while the low-temperature WHIM with $T < 10^5$ K contributes ~55%–60% of the O VI and O V absorption systems. (3) Finally, the emission lines from oxygen ions were calculated. They are emitted mostly from collisionally excited ions. We estimate that ~95% of the O VII line (574 eV) and O VIII line (653 eV) emission comes from the WHIM with $10^6 < T < 10^7$ K, while ~75% of the O VI line (1032 Å) and ~80% of the O V line (630 Å) are emitted by the WHIM with $10^5 < T < 10^6$ K. Hence, we conclude that *absorption systems in UV due to species such as* O V *and* O VI *provide the best chance to detect the low-temperature WHIM with* $T < 10^5$ K.

H. K. and D. R. were supported in part by KOSEF through the Astrophysical Research Center for the Structure and Evolution of Cosmos (ARCSEC) and grant R01-1999-00023. H. K. and D. S. were supported in part by a grant at Korea Astronomical Observatory. Numerical simulations utilized "The Grand Challenge Program" of the KISTI Supercomputing Center. We thank T. W. Jones, E. Hallman, and R. Benjamin for discussions and the anonymous referee for constructive comments.

REFERENCES

Bennett, C. L., et al. 2003, ApJS, 148, 1
Bergeron, J., Aracil, B., Petitjean, P., & Pichon, C. 2002, A&A, 396, L11
Cen, R., Kang, H., Ostriker, J. P., & Ryu, D. 1995, ApJ, 451, 436
Cen, R., & Ostriker, J. P. 1999a, ApJ, 514, 1
———. 1999b, ApJ, 519, L109
Cen, R., Tripp, T. D., Ostriker, J. P., & Jenkins, E. B. 2001, ApJ, 559, L5
Chen, X., Weinberg, D. H., Katz, N., & Davé, R. 2003, ApJ, 594, 42
Davé, R., et al. 2001, ApJ, 552, 473
Dopita, M. A., & Sutherland, R. S. 2003, Astrophysics of the Diffuse Universe (Berlin: Springer)
Fang, T., & Bryan, G. L. 2001, ApJ, 561, L31
Fang, T., Croft, R. A. C., Sanders, W. T., Houck, J., Dave, R., Katz, N., Weinberg, D. H., & Hernquist, L. 2005, ApJ, in press (astro-ph/0311141)
Ferland, G. J., Korista, K. T., Verner, D. A., Ferguson, J. B., Kingdon, J. B., & Verner, E. M. 1998, PASP, 110, 761
Finoguenov, A., Briel, U. G., & Henry, J. P. 2003, A&A, 410, 777
Frenk, C. S., et al. 1999, ApJ, 525, 554
Fukugita, M. 2004, in IAU Symp. 220, Dark Matter in Galaxies, ed. S. D. Ryder et al. (San Francisco: ASP), 227
Fukugita, M., Hogan, C. J., & Peebles, P. J. E. 1998, ApJ, 503, 518
Furlanetto, S. R., & Loeb, A. 2004, ApJ, 611, 642
Furlanetto, S. R., Schaye, J., Springel, V., & Hernquist, L. 2003, ApJ, 599, L1
Gabici, S., & Blasi, P. 2003, ApJ, 583, 695
Hellsten, U., Gnedin, N. Y., & Miralda-Escudé, J. 1998, ApJ, 509, 56
Hui, L., & Gnedin, N. Y. 1997, MNRAS, 292, 27
Kang, H., Cen, R., Ostriker, J. P., & Ryu, D. 1994a, ApJ, 428, 1
Kang, H., Ostriker, J. P., Cen, R., Ryu, D., Hernquist, L., Evrard, A. E., Bryan, G. L., & Norman, M. L. 1994b, ApJ, 430, 83
Kang, H., Ryu, D., & Jones, T. W. 1996, ApJ, 456, 422
LeVeque, R. J. 1997, in Computational Methods in Astrophysical Fluid Flows, ed. O. Steiner & A. Gautschy (Berlin: Springer), 1
McKernan, B., Yaqoob, T., Mushotzky, R., George, I. M., & Turner, T. J. 2003, ApJ, 598, L83
Mewe, R., Gronenschild, E. H. B. M., & van den Oord, G. H. J. 1985, A&AS, 62, 197
Miniati, F., Ryu, D., Kang, H., Jones, T. W., Cen, R., & Ostriker, J. 2000, ApJ, 542, 608
Miyaji, T., Ishisaki, Y., Ogasaka, Y., Ueda, Y., Freyberg, M. J., Hasinger, G., & Tanaka, Y. 1998, A&A, 334, L13
Nicastro, F., et al. 2003, Nature, 421, 719
Ohashi, T., et al. 2004, preprint (astro-ph/0402546)
Phillips, L. A., Ostriker, J. P., & Cen, R. 2001, ApJ, 554, L9
Quilis, V., Ibanez, J. M. A., & Saez, D. 1998, ApJ, 502, 518
Ryu, D., Kang, H., Hallman, E., & Jones, T. W. 2003, ApJ, 593, 599
Ryu, D., Ostriker, J. P., Kang, H., & Cen, R. 1993, ApJ, 414, 1
Shull, J. M., Roberts, D., Giroux, M. L., Penton, S. V., & Fardal, M. A. 1999, AJ, 118, 1450
Spergel, D. N., et al. 2003, ApJS, 148, 175
Sutherland, R. S., & Dopita, M. A. 1993, ApJS, 88, 253
Valageas, P., Schaeffer, R., & Silk, J. 2002, A&A, 388, 741
Viel, M., Branchini, E., Cen, R., Matarrese, S., Mazzotta, P., & Ostriker, J. P. 2003, MNRAS, 341, 792
Yoshikawa, K., Yamasaki, N. Y., Suto, Y., Ohashi, T., Mitsuda, K., Tawara, Y., & Furuzawa, A. 2003, PASJ, 55, 879
Zappacosta, L., Maiolino, R., Mannucci, F., Gilli, R., Finoguenov, A., & Ferrara, A. 2004a, preprint (astro-ph/0401202)
Zappacosta, L., Maiolino, R., Mannucci, F., Gilli, R., & Schuecker, P. 2004b, MNRAS, in press (astro-ph/0402575)